TECHNICAL REPORT ARLCD-TR-82026

CARS SPECTRA
FROM LEAN AND STOICHIOMETRIC CH(4)-N(2)0 FLAMES

L. E. HARRIS

MARCH 1983

US ARMY ARMAMENT RESEARCH AND DEVELOPMENT COMMAND
LARGE CALIBER
WEAPON SYSTEMS LABORATORY
DOVER, NEW JERSEY

UNCLASSIFIED

SECURITY CLASSIFICATION OF THIS PAGE *(When Data Entered)*

REPORT DOCUMENTATION PAGE		READ INSTRUCTIONS BEFORE COMPLETING FORM
1. REPORT NUMBER Technical Report ARLCD-TR-82026	2. GOVT ACCESSION NO.	3. RECIPIENT'S CATALOG NUMBER
4. TITLE *(and Subtitle)* CARS SPECTRA FROM LEAN AND STOICHIOMETRIC CH(4)-N(2)O FLAMES		5. TYPE OF REPORT & PERIOD COVERED 6. PERFORMING ORG. REPORT NUMBER
7. AUTHOR*(s)* L.E. Harris		8. CONTRACT OR GRANT NUMBER*(s)*
9. PERFORMING ORGANIZATION NAME AND ADDRESS ARRADCOM, LCWSL Applied Sciences Div (DRDAR-LCA-G) Dover, NJ 07801		10. PROGRAM ELEMENT, PROJECT, TASK AREA & WORK UNIT NUMBERS 1L16122AH60
11. CONTROLLING OFFICE NAME AND ADDRESS ARRADCOM, TSD STINFO Div (DRDAR-TSS) Dover, NJ 07801		12. REPORT DATE March 1983 13. NUMBER OF PAGES 46
14. MONITORING AGENCY NAME & ADDRESS*(if different from Controlling Office)*		15. SECURITY CLASS. *(of this report)* Unclassified 15a. DECLASSIFICATION/DOWNGRADING SCHEDULE

16. DISTRIBUTION STATEMENT *(of this Report)*

Approved for public release; distribution unlimited.

17. DISTRIBUTION STATEMENT *(of the abstract entered in Block 20, if different from Report)*

18. SUPPLEMENTARY NOTES

Portions of this report are extracted from Technical Report ARLCD-TR-82020, "Broadband N(2) and N(2)O CARS Spectra from a CH(4)-N(2)O Flame", December 1982, L.E. Harris.

19. KEY WORDS *(Continue on reverse side if necessary and identify by block number)*

Broadband CARS
CARS spectra
Spectroscopy

20. ABSTRACT *(Continue on reverse side if necessary and identify by block number)*

Broadband CARS spectra were obtained from both the reaction zone and post-flame region of lean and stoichiometric CH(4)-N(2)O flames. To assess methods of obtaining concentration from broadband spectra, N(2) CARS spectra were obtained from a series of air and argon (AIR/AR) mixtures at room temperature. The concentration of N(2) with good accuracy (6%) was obtained both from fitting the shape of the broadband spectra and from the ratio of the resonant to nonresonant susceptibility. Both methods were utilized in interpreting flame spectra.

(cont)

DD FORM 1 JAN 73 1473 EDITION OF 1 NOV 65 IS OBSOLETE

UNCLASSIFIED

SECURITY CLASSIFICATION OF THIS PAGE *(When Data Entered)*

20. ABSTRACT (cont)

CARS spectra of both N(2) and N(2)O were obtained from the reaction zone of near 0.3 equivalence ratio (fuel/oxidizer) CH(4)-N(2)O flames. Spectra were obtained from room temperature to near the adiabatic flame temperature. Simultaneous observation of both N(2) and N(2)O spectra allows determination of temperature and concentration of both species from the same point in the flame. The spectra demonstrated the high spatial resolution of CARS.

In addition, N(2) CARS spectra were obtained from the post-flame region of 0.3, 0.4, 0.5 and 1.0 CH(4)-N(2)O flames. The N(2) spectra were used to obtain concentration and temperature profiles by a least squares fit to model calculations. The temperatures obtained varied with reactant flow rates. However, at appropriate flow rates, the concentrations and temperatures obtained close to the burner surface were in accord with thermochemical calculation.

The temperature and concentration profiles obtained from both N(2) and N(2)O CARS spectra can be used to understand the elementary processes occurring in the CH(4)-N(2)O flames investigated.

CONTENTS

TABLES

FIGURES

INTRODUCTION

Recently, coherent anti-stokes raman scattering (CARS) spectroscopy has undergone several modifications to enhance its usefulness for investigating flames. CARS can arise from the nonlinear response of homogeneous media. The nonlinear response of a homogeneous medium upon which waves ω_1 and ω_2 are incident generates an oscillating polarization. The lowest order nonlinearity is the third order susceptibility, $\chi^{(3)}(-\omega_3, \omega_1, \omega_1, \omega_2)$, which generates a frequency component of the polarization at $\omega_3 = 2\omega_1 - \omega_2$ by the process termed "three wave mixing" (ref 1). Resonant enhancement of three wave mixing occurs if $\omega_1 - \omega_2$ is made equal to a Raman active vibration, ω_v, in which case the enhancement of the signal ω_3 is termed a CARS process (ref 2). Since CARS is a coherent process, ω_3 is maximized if the wavevectors, k_i, are phasematched so that $2k_1 = k_2 + k_3$ where k_i equals $\omega_i n_i/c$, c the speed of light, and n_i the refractive index at frequency ω_i. In gases, which are nearly dispersionless, colinear beams are phasematched. Using this geometry, since CARS is generated by an iterative growth process, the spatial resolution is poor. If ω_1 is split and phasematching achieved, ω_3 is maximized and, since CARS generation occurs only where all three beams intersect, the spatial resolution is improved. The split ω_1 phasematched geometry is termed "BOXCARS" (ref 3). BOXCARS in which the wavevectors are not phasematched in one plane is termed folded (or nonplanar) BOXCARS and has the advantage that ω_3 is easily spatially isolated from the generating beams (refs 4 through 6).

Conventionally ω_2 is narrowband and scanned to obtain the spectrum at ω_3. However, to obtain spectra in transient and/or turbulent media it is appropriate to use a broadband ω_2 [~150 cm^{-1} full width at half height (FWHH)] to obtain the full rovibrational spectrum at ω_2 within the time duration of the laser pulse (~10 ns) (ref 7). Averaging of the single-shot spectra may be undertaken to improve the signal-to-noise according to the constraints of the experiment.

BOXCARS has been used to obtain temperature and concentration of post-flame gases in stationary flames using broadband (ref 8) and narrow band (ref 9) spectra, and transient flames using single-shot (ref 10) spectra. Recently, laser absorption measurements of the temperature and concentration of radicals have been reported in the thin reaction zone of atmospheric flames (ref 11). CARS measurements in the reaction zone of a flame have not been reported even though BOXCARS has more precisely defined spatial resolution in the direction of the laser beams than line-of-sight methods such as laser absorption. In addition CARS allows direct monitoring of the rovibrational levels of the reactant molecules as they undergo flame decomposition processes.

Because of these capabilities, simultaneous measurement of N_2 and N_2O CARS was undertaken in the reaction zone of a lean CH_4-N_2O flame. A lean CH_4-N_2O flame near lift-off creates sufficiently sharp spatial and temperature gradients to show the capabilities of CARS. N_2O CARS spectra, which have not been previously reported, have structure at lower temperatures than diatomics due to the population of low-lying bending modes. N_2O CARS spectra are especially suitable for studying initial decomposition reaction in a CH_4-N_2O flame. The measurements were extended for N_2 CARS to the post flame region of a series of flames with equivalence ratio increasing to 1.0 to evaluate the agreement of temperatures and

concentrations determined from CARS spectra with the results of thermochemical calculations (ref 12).

EXPERIMENTAL METHOD

CARS spectra were generated using the apparatus shown in figure 1. Non-planar BOXCARS was utilized to achieve phasematching. The output of a Quanta-Ray DCR-1A Nd/YAG laser at 1.06 microns (700 mj) is doubled to generate the pump beam at 5320 Å (250 mj) with a bandwidth near 1 cm^{-1}. The pump beam is separated from the primary beam using prisms. The pump beam is split using beam splitter BS1 to generate $\omega_1 p$ and $\omega_1 s$. $\omega_1 s$ is used to pump a dye laser to generate the Stokes beam, ω_2. The dye laser consists of a flowing dye cell in a planar Fabry-Perot oscillator cavity pumped slightly off-axis by 20% of $\omega_1 s$ with the output amplified by an additional dye cell pumped by the remainder of $\omega_1 s$. The dye laser was operated broadband using Exciton Rhodamine 640 in dry methanol at a concentration of 2.4×10^{-4} M and 3.2×10^{-5} M in the oscillator and amplifier dye cell, respectively, to produce 30 mj centered at 6060 Å (16502 cm^{-1}) with a bandwidth of 121 cm^{-1}. To achieve BOXCARS geometry, $\omega_1 p$ is again split with beam splitter, BS2, to generate ω_1 and ω_1'. In the optical configuration used to generate non-planar BOXCARS, the ω_1, ω_1', and ω_2 beams are parallel and situated on a circle of 1 inch diameter at the focusing lens (200 mm focal length) with ω_1 and ω_1' in the central horizontal plane of the lens and ω_2 below ω_1 and ω_1' in the central vertical plane. Telescopes are inserted in the $\omega_1 p$ and ω_2 beams to allow the focal spot size of both beams to be equalized. The telescopes also allow the position of the ω_1, ω_1', and ω_2 beamwaists to be adjusted so that they all intersect after focusing. This was achieved using 0.85 and 2x Galilean telescopes in $\omega_1 p$ and ω_2, respectively. To achieve phasematching a 12.5 mm thick optical flat rotatable about it's horizontal axis was inserted into ω_2 before focusing. It is adjusted to maximize the ω_3 signal. The beams were recollimated with a lens (200 mm focal length) after which the ω_3 was located below the plane of ω_1 and ω_1'. ω_1, ω_1', and ω_2 were terminated with a neutral density filter (OD4). ω_3 was focused using a 50 mm focal length lens onto the slits of a 1/4-meter monochromator equipped with a 1,800 line per millimeter grating and 100-micron slits. The signal was detected by a PAR SIT detector and processed by a PAR OMA2 system. Neon lines were used to calibrate the monochrometer. The FWHH of the Neon lines nearest ω_3 were determined to be 6.4 cm^{-1} with 2.33 cm^{-1} per channel.

Flame measurements were made on a premixed CH_4-N_2O flame maintained on a circular burner of 1.4 cm diameter. The burner surface was constructed of a matrix of steel syringe needles of 0.2 cm outer diameter so that a flat flame is obtained under suitable flow conditions. Matheson technical grade methane and chemically pure nitrous oxide were separately flowed through Matheson rotameters prior to premixing. The flow through the burner was adjusted to 16.1 cm/s to maintain a 0.27 fuel-air equivalence ratio flame, which is near lift-off, localized at a few syringe tubes near the center of the burner. The oblong shaped flame increased in size to approximately 5 mm in diameter at 10 mm above the burner surface. Increasing the methane flow to that for a 0.31 equivalence ratio flame gave a flat flame at a flow of 16.3 cm/s. The flow conditions for the other flames used are given in the results section. The center line of the burner was placed at the intersection of the ω_1, ω_1', and ω_2 beamwaists. The burner was mounted on horizontal and vertical translation stages.

RESULTS

Theory

N_2 CARS spectra were calculated using the method outlined in reference 13 and N_2 spectral parameters given in references 13 and 14. The observed CARS spectrum is proportional to the square of the modulus of the third order susceptibility, $\chi^{(3)}$, which is the sum of a resonant term, χ_r, related to a nuclear displacement and a nonresonant term, χ_{nr}, related to electronic displacement.

$$\chi^{(3)} = \chi_r + \chi_{nr} \tag{1}$$

The resonant term is calculated as a sum of Lorentian line shapes of each Q(J) rotational transition

$$\chi_r = \sum_j \frac{kj\ \Gamma j}{2\Delta\omega_j - i\Gamma_j} \tag{2}$$

given that

$$kj = \frac{2N}{\hbar} / \alpha_j /^2 (\Delta p_j^{(o)})\ \Gamma_j^{-1} \tag{3}$$

where N is the number density, α_j is the isotropic polarizability matrix element for the transition, $\Delta p_j^{(o)}$ is the normalized population difference between the molecular energy levels involved in the transition, Γ, is the isolated pressure-broadened linewidth, and $\Delta\omega_j = \omega_1 - \omega_2 - \omega_j$. The calculated $/\chi^{(3)}/2$ is first convoluted over the laser shapes and then over a triangular instrumental slit function.

χ_r is the sum of real and imaginary components χ' and χ'', respectively, so that

$$/\chi^{(3)}/^2 = \chi'^2 + 2\chi'\chi_{nr} + \chi''^2 + \chi_{nr}^2 \tag{4}$$

χ' and χ'' display resonant and dispersive behavior with respect to the detuning frequency, $\Delta\omega_j$.

As the concentration of the resonant species is lowered the cross term $\chi'\chi_{nr}$, which is dispersive, modulates the shape of the spectrum. The observation of dispersively modulated spectra allows estimation of the concentration in addition to the temperature based on model calculations.

As an alternative to determining concentration from the shape of the total spectrum, concentration can be estimated from the ratio of the total CARS intensity, I, to the nonresonant intensity, Inr, at any frequency at which a resonant transition of the species occurs. In broadband CARS the nonresonant susceptibility is usually observed directly in regions where no resonance occurs. The spectral distribution of the nonresonant susceptibility which mirrors that of ω_2, can be obtained either from measurements of the distribution of ω_2 or directly from

measurements on a nonresonant gas. The spectral distribution of the nonresonant susceptibility is relatively constant (as can be ascertained by measurements before and after a series of experiments). Therefore, measurement of the nonresonant susceptibility at any frequency in the broadband spectrum will allow estimation of Inr, the nonresonant susceptibility at the frequency at which the intensity of the resonant transition, I, occurs. The function (I-Inr)/Inr should be independent of the laser intensity (although of course the precision will be affected by the intensity) and according to equations 2 and 3 vary with concentration, quadratically at high concentration and linearly at lower concentration when $\chi''^2 << 2\chi'\chi_{nr}$. If Inr is estimated at a frequency at which the nonresonant susceptibility begins to have some significant contribution from the resonant susceptibility at higher concentrations a lowering of the quadratic dependence would be observed. This effect would depend on the ratio of the resonant to nonresonant susceptibility cross section for the system under investigation. The effect would be minimized by proper choice of the frequency at which the nonresonant susceptibility is determined.

Air/Argon Mixtures

N_2 CARS spectra were taken at 2 mm above the burner head of mixtures of room temperature premixed air and argon (AIR/AR) flowing through the burner. The composition of the AIR/AR mixtures was set by adjusting the flow of argon and air separately prior to premixing. The total flow for argon was at a rate at which no signal was observed from nitrogen diffusing into the argon flow from the surrounding air. The percentage of air in the mixtures varied from 0% to 30%. The spectra of the mixtures are shown in figures 2 and 3. The compositions of the mixtures for which N_2 CARS spectra were taken are given in table 1. CARS spectra for which the air concentrations were determined from a fit of the total spectra to the calculated spectra are shown in figures 4 and 5. The concentration determined by the best visual match between the calculated and experimental spectra were 9% and 20% air for gas mixtures whose compositions were 8.54% and 19.7%, respectively.

Concentrations determined from the function (I-Inr)/Inr are given in table 1. I was determined from the intensity of the broadband CARS spectra at the frequency of the maximum of the nitrogen Q_{10} resonance. Inr, which was 80% of the peak nonresonant susceptibility at the frequency of I, was determined from the intensity in the broadband spectra at the frequency at which the nonresonant susceptibility is 80% of the peak value on the other side of the peak of the nonresonant susceptibility curve from that at which the nitrogen resonance occurs to avoid interference from the resonant susceptibility.

The values calculated for (I-Inr)/Inr are shown in figure 6 along with (I-Inr)/Inr determined from model spectra. The calculated and experimental log (I-Inr)/Inr agreed closed as can be seen from figure 6. The percent of air in the mixtures (table 1) was determined from the theoretical curve given in figure 6. For higher concentration the slope of the curve is near two. The slope as expected decreases for lower concentration. The agreement between the experimentally determined and known percent of air was 6.1%. In this method of determining composition it is not necessary to obtain a calibration curve since the experimental and theoretical spectra are in good agreement. In addition, this

method offers rapid data reduction of large amounts of data with reasonable accuracy. Fitting the full spectrum by a least squares method should give increased precision.

Reaction Zone Spectra

Broadband N_2 and N_2O spectra were obtained from the reaction zone of both the 0.27 and 0.30 equivalence ratio flames. In addition, N_2 spectra were obtained in the post-flame region of these flames. The 0.27 equivalence ratio flame was scanned horizontally from the outer wall of the burner to the centerline at a height of 1 mm above the burner surface. N_2 and N_2O spectra obtained from the region of largest concentration and temperature gradient prior to the disappearance of N_2O are shown in figure 7. The 0.30 equivalence ratio flame, which was a flat flame, was scanned vertically along the center line. Spectra similar to that shown in figure 7 were obtained below the region of maximum temperature.

To identify N_2O CARS spectra, which had not been reported previously, CARS spectra were also taken 1 mm above the centerline of the burner with room temperature N_2O gas flowing through the burner at a velocity sufficient to remove N_2 from the sampling volume. Spectra were taken above both a room temperature burner and a burner heated by heat transfer from a flame extinguished immediately prior to the measurement. The room temperature N_2O spectra had a prominent peak at 2224.7 cm^{-1} with a low intensity shoulder at 2208.8 cm^{-1}. The spectra taken above the hot burner showed four peaks of progressively diminishing intensity at 2224.7, 2208.8, 2192.8, and 2174.7 cm^{-1}. Similar peaks have been observed at 2223.8, 2209.5, and 2195.6 cm^{-1} in the infrared and Raman at 337 K and assigned to ν_3, $\nu_3 + \nu_2 - \nu_2$ and $\nu_3 + 2\nu_2 - 2\nu_2$ where ν_1, ν_2, and ν_3 are the NO stretch at 1285, the bend at 558.8 and the NN stretch at 2223.5 cm^{-1}, respectively (ref 15). The positions of ν_3, $\nu_3 + \nu_2 - \nu_2$, $\nu_3 + 2\nu_2$ and $\nu_3 + 3_2 - 3_2$, using Susuki's values (ref 16) for the spectroscopic constants are calculated to occur at 2223.5, 2201.5, 2195.3, and 2180.3 cm^{-1} in good agreement with the N_2O peak position observed in the spectrum taken above the hot burner. The spectra taken in the flame (fig. 7) show, in addition to a peak attributable to the N_2 Q branch fundamental, Q_{10}, at 2330 cm^{-1} and associated hot bands, the same peaks that occur in N_2O above the hot burner. An expanded version of the spectrum taken 1.4 mm from the centerline is shown in figure 8. This spectrum clearly shows the resolved structure of hot N_2O.

The spectra shown in figure 7 and similar spectra taken at other positions in the flame allow the determination of temperature and concentration of N_2 and N_2O. Comparison of the half width of the nitrogen Q_{10} transition and the modulation of spectra by the nonresonant susceptibility with model calculations allows the estimation of temperature to ±100 K and concentration to ±10% when no hot bands are observed. Observation of hot bands allows least squares fitting of the calculated and experimental Q peak maxima to give temperature to ±50 K and concentration to ±5% based on replicate determinations. Calculated spectra are shown in figures 8 and 9. The temperature and concentrations estimated for the 0.27 flame are given in table 2.

In addition, the concentration of N_2O can be estimated from the resonant and nonresonant intensity at ν_3 as discussed. Knowing the spectrum of the nonresonant susceptibility, the nonresonant intensity at ν_3 can be obtained from each broadband spectrum. The square root of the ratio of the resonant to nonresonant intensity, which is linear with concentration, was used to obtain N_2O concentration utilizing the broadband N_2O spectrum at room temperature for calibration. In this case experimental calibration is needed since the N_2O CARS spectra were not calculated. (The effect of temperature, which was small since both the resonant and nonresonant susceptibility scale similarily with temperature, was determined from model calculations). Having obtained the concentration of N_2O, the N_2 concentration can be obtained from the ratios of N_2 to N_2O intensity (fig. 10) taking into account that resonant cross section of N_2O is 0.53 that of N_2 (ref 17).

Post-Flame Spectra

The agreement of temperature and concentration obtained from N_2 CARS spectra with the results of thermochemical calculations (table 3) was investigated in the post-flame gases of lean and stoichiometric flames. Temperature and concentration were determined along the centerline of the burner as a function of distance above the burner. The temperature as indicated by the height of the Q_{21} and Q_{32} nitrogen hot bands increased with the rate of flow. As discussed, in a 0.3 flame at 2 mm above the burner N_2O was observed along with N_2. At 3 mm and 4 mm above the burner surface, N_2 was observed at temperatures of 2350 K and 2453 K, respectively. At 5 mm the temperature and concentration (table 2) were determined from the spectra shown in figure 9. Above 5 mm (up to 6 cm) the temperature decreased while the concentration remained constant within experimental error. In lean and stoichiometric flames investigated with equivalence ratios higher than 0.3, at sufficiently high flow rates, N_2O was not observed and Q_{21} and Q_{32} N_2 relative heights indicated temperatures substantially above the values given by the thermochemical calculations with Q_{32} indicating temperatures higher than Q_{21} and up to 4000 K in some instances. The cause of these anomalous spectra is presently being investigated. At lower flow rates the spectra (fig. 11) obtained 2 mm above the burner surface in 0.4, 0.5 and 1.0 flames in addition to the 0.3 at 5 mm, gave temperatures and concentrations (table 4) consistent with the thermochemical calculations.

The experimental precision of the temperatures and concentrations was determined by comparison of four replicate measurements on the 1.0 flame. The error determined in this manner is consistent with the photon statistics of the measurements. The percent error in the measurements for the other flames should be similar since all the spectra were summed (200 scans) to give near to 10,000 counts at Q_{10}.

At a lower flow rate in the 0.5 flame lower temperatures were obtained. The profiles in the 0.5 flame at flows of 16.9 and 33.4 cm/s are given in tables 5 and 6, respectively. The N_2 spectra at the higher flow are shown in figures 12 and 13. A comparison of the differing profiles is given in figure 14. In the 1.0 flame, lower flame velocity resulted in flashback before any lowering in measured temperature was observed.

To summarize, in the 0.3 flame close to the burner surface (1 mm above) N_2O spectra along with N_2 spectra were observed. Higher above the burner surface (5 mm) a maximum temperature and concentration in agreement with thermochemical calculations was observed. In the 0.4 flame at the same flow, 16.8 cm/s and position in the flame N_2O was not observed and the measured temperature and concentration are in close agreement with theory. In the 0.5 flame at nearly the same flow temperatures lower than theory are measured. At sufficiently high flow, 56.7 and 60.5 cm/s in the 0.5 and 1.0 flames, respectively, anomalous spectra giving apparent temperature much higher than theory were encountered. In the 0.5 and 1.0 flames, at flow intermediate between striking back and those at which anomalous spectra were encountered, the temperature and concentration were consistent within experimental error with theory. The intermediate range of flows at which agreement with theory was obtained increased with the calculated flame temperature as the equivalence ratio was increased toward 1.0.

DISCUSSION

Measurements were made in AIR/AR mixtures to assess the use of CARS to determine concentration. Visually matching the shape of modulated CARS spectra with the results of model calculations for 9% and 20% AIR mixtures gives results within the accuracy of the flow meters (5%). A least squares fit of all the points would improve the precision. Alternately, comparing the experimental function (I-Inr)/Inr obtained from two experimental points with the theoretical function (I-Inr)/Inr versus concentration also allows evaluation of the concentration to close to the accuracy of the flow meters. These methods of obtaining concentration were used in obtaining the reaction zone and post-flame region results.

CARS N_2O spectra obtained above both room temperature and heated burner heads are in good agreement with previously reported Raman and infrared spectra (ref 15) and with the results of calculations made using the spectral constants of Suzuki (ref 16). CARS N_2O spectra has the advantage of having structure useful for making measurements of temperature and concentration at much lower temperatures than diatomics such as nitrogen. From the temperature obtained from N_2 spectra (table 2) the normalized intensity of the N_2O $\nu_3 + \nu_2 - \nu_2$ band relative to ν_3 is greater than 0.1 above 600 K, whereas the normalized intensity of the N_2 Q_{21} band does not reach 0.1 until the temperature exceeds 1500 K. The higher intensity of the N_2O $\nu_3 + \nu_2 - \nu_2$ band arises from the low energy and double degeneracy of the ν_2 vibration. Thus N_2O and similar triatomics are especially valuable for characterizing the lower temperature regions of the profiles obtained in the 0.27 flame. In this region the N_2 spectra were not sufficiently intense to precisely estimate temperature. The complete modeling of N_2O CARS spectra which is now underway will allow these calculations to be made.

The simultaneous observation of N_2 spectra along with N_2O spectra allows determination of N_2 to N_2O relative concentration, N_2 and N_2O temperature and concentration. The random error in the N_2O resonant to nonresonant intensity ratios depend solely on the photon statistics of the measurements. (In the worst case the resultant error would be 5% in N_2 concentration). The accuracy of the N_2 concentrations determined from the relative intensity of N_2 to N_2O also depends on the relative ratios of the Raman cross sections. The N_2 temperature and

concentrations determined from the shape of the N_2 CARS signal depends on the N_2 spectral parameters and the spectral simulation model which together have been estimated to give errors of ±100 K at low temperature and 10% in concentration in flames when only N_2 0_{10} is observed. The average difference between N_2 concentration determined from intensity ratio and band shape is only 10% which is consistent with the estimated error in the methods used. When additional hot bands are observed the precision is increased to ±50 K in temperature and 5% in concentration.

The data in figure 10 give insight into the chemical and physical processes occurring in the very spatially inhomogeneous 0.27 flame. N_2 from the surrounding air diffuses into the flame for a distance of approximately 2 mm at which point N_2 CARS spectra is no longer observed (fig. 10). N_2 is again observed when measurements are made closer than 2.3 mm from the centerline of the flame. The $(N_2/N_2O)^{\frac{1}{2}}$ ratio then rises exponentially as measurements closer to the flame are made with a concomitant rise in temperature.

H_2-N_2O flames have been studied in detail using mass spectometric means to obtain concentration (ref 18). From these studies it is suggested that the H_2-N_2O flame has a two-stage reaction zone. In the first stage (T<1700 K) the kinetics follow the usual bimolecular elementary steps of the hydrogen-oxygen system:

$$H_2 + OH \rightarrow H_2O + H \qquad \text{r. 1}$$

$$H_2 + O \rightarrow OH + H \qquad \text{r. 2}$$

$$H + O_2 \rightarrow OH + H \qquad \text{r. 3}$$

plus reaction

$$H + N_2O \rightarrow N_2 + OH \qquad \text{r. 4}$$

where $k_4 = 6 \times 10^{13} \exp(-13100/RT) cm^3\ mole^{-1}s^{-1}$ all these reactions are characterized by a relatively low activation energy.

The second stage (T>1700 K) is dominated by the unimolecular decomposition of N_2O

$$N_2O + M \rightarrow N_2 + O + M \qquad \text{r. 5}$$

where $k_5 = 1.3 \times 10^{15} \exp(-56500/RT)$. Molecular oxygen is produced via

$$N_2O + O \rightarrow N_2 + O_2 \qquad \text{r. 6}$$

and NO via

$$N_2O + O \rightarrow 2NO \qquad \text{r. 7}$$

where $k_6 = 5.4 \times 10^{14} \exp(-32000/RT) cm^3\ mole^{-1}s^{-1}$ with $k_6/k_7 = 3.2$.

The data given in table 2 and figure 10 are consistent with the kinetics proposed above for stage one, in that N_2 is observed to occur at temperatures below the 1700 K at which the stage two reactions become significant. Thus reaction 4 is seen as a possible source of the N_2 observed at low temperature in the CH_4-N_2O flame. Further kinetic analysis particularly dependent on temperature and concentration from N_2O spectra, will determine whether reaction 4 can quantitatively account for the N_2 and N_2O profiles observed in the CH_4-N_2O flame.

In the post-flame region the variation of measured temperature with flow can be partially accounted for by the variation of the position of the reaction zone with respect to the burner as a function of flow. In the 0.3 flame, the burning velocity is sufficiently low to be displaced by a flow of 16.8 cm/s above the burner surface to allow observation of N_2O spectra from the reaction zone. As the burning velocity increases for the flames with increased equivalence ratio the flow is not sufficient to allow observation of N_2O; however, temperature is observed to increase with flow which indicates that the reaction zone is displaced sufficiently above the burner surface to inhibit heat lost to the burner. The displacement of the reaction zone above the burner surface so that heat loss to the surface is inhibited is consistent with the agreement within experimental error of the measured and calculated flame temperatures (refs 19 and 20). The anomalously high temperature indicated at still higher flows is perhaps related to distortion of the reaction zone by turbulence induced by the high flow (refs 19 and 20). Further work is needed to interpret the spectra at high flow.

Broadband CARS has been shown to provide temperature and concentration with good precision for major flame species which can perhaps be extended to transients with resonance enhancement. The spatial resolution of the technique was adjusted to obtain information from the thin resolution zone (<1 mm) of the atmospheric CH_4-N_2O flame. The technique also has the potential for time resolved single shot (10 ns) measurements for use in transient media. These capabilities as has been shown in the CH_4-N_2O flame can be used to obtain information on the elementary reactions occurring in both transient and stationary flames.

REFERENCES

1. N. Bloembergen, Nonlinear Optics, Benjamin, New York, 1965.

2. B. I. Greene, R. B. Weisman and R. M. Hochstrasser, Chem Phys, Letters 59, 1978, p 5.

3. A. C. Eckbreth, Appl Phys, Letters 32, 1978, p 421.

4. R. L. Farrow, P. L. Mattern and L. A. Rahn, Sandia Laboratories Report 80-8640, 1980.

5. J. A. Shirley, R. J. Hall and A. C. Eckbreth, Opt Letters 5, 1980, p 380.

6. Y. Prior, Appl. Opt. 19, 1980, p 1741.

7. W. B. Roh, P. W. Schreiber and J. P. E. Taran, Appl. Phys., Letters 29, 1976, p 174.

8. A. C. Eckbreth and R. J. Hall, Combustion Science and Technology, vol 25, 1981, p 175.

9. K. Muller - Dethlefs, M. Pealat and J. P. E. Taran, Ber. Bunsenges Phys. Chem., vol 85, 1981, p 803.

10. L. E. Harris and M. E. McIlwain, Combustion and Flame, vol 48, 1982, p 97.

11. M. S. Chou, A. M. Dean and D. Stern, J. Chem Phys, vol 76, 1982, p 5334.

12. S. Gordon and B. J. McBride, "Computer Program for Calculation of Complex Chemical Equilibrium Compositions, Rocket Performance, Incident and Reflected Shocks, and Chapman-Jouquet Detonations," NASA SP-273, 1976.

13. R. J. Hall, Combustion Flame, vol 35, 1979, p 47.

14. A. Owyoung and L. A. Rahn, J. Quant. Elect., vol QE15, 1979, p 25D.

15. C. Dreyfus, L. Berreby and T. Nguyen - Tan, J. Chem Phys, vol 76, 1982, p 755.

16. I. Suzuki, J. Mol. Spectry., vol 32, 1969, p 54.

17. D. G. Fouche and R. K. Chang, Appl. Phys., Letters 20, 1972, p 256.

18. V. P. Balakhnine, J. Vandooren and P. J. Van Tiggelen, Combustion Flame, vol 28, 1977, p 165.

19. A. G. Gaydon and H. G. Wolfhard, Flames, John Wiley, New York, 1969, pp 92-146.

20. I. Glassman, Combustion, Academic Press, New York, 1977, pp 87-105.

Table 1. Concentration of air (%) in air/ar mixtures at 300 K

Concentration		Difference between columns 1 and 2	% Difference between columns 1 and 2
Experimental (%)	Calculated (%)		
7.06	5.92	1.1	16.1
8.54	7.80	0.7	8.7
12.0	11.6	0.4	3.3
13.8	14.8	-1.0	7.2
19.7	18.8	0.9	4.5
22.8	22.7	0.1	0.50
30.2	31.0	-0.8	2.65
Mean (σ)		0.7 (0.3)	6.1 (5.1)

Table 2. Temperature and concentration in the reaction zone of a CH_4-N_2O flame (2 mm above the burner)

Distance from flame center (mm)	Concentration from intensity (%)		Concentration and temperature from N_2 spectral shape	
	N_2O	N_2	N_2(%)	T(K)
0			33	2300
1.14	0	--	20	1200
1.27	20	19	17	900
1.40	28	15	14	800
1.52	43	11	10	600
1.65	58	9.4		
1.78	69	7.9		
2.03	83	6.0		
2.16	93	--		

Table 3. Thermochemical calculations for CH_4-N_2O flames

ϕ / Species	0.1	0.3	0.4	0.5	0.7	1.0
	Composition (%)					
CO	0.02	0.43	0.99	1.77	3.80	7.35
CO_2	1.62	4.28	5.14	5.69	6.09	5.66
H	--	0.11	0.27	0.50	1.14	2.30
H_2	--	0.14	0.32	0.59	1.43	3.55
H_2O	3.13	8.46	10.66	12.60	15.90	19.30
N_2	64.82	61.64	60.03	58.40	55.40	51.28
NO	1.33	2.25	2.42	2.43	2.17	1.48
O	0.12	0.79	1.21	1.54	1.87	1.58
OH	0.27	2.53	2.27	2.93	3.81	4.02
O_2	28.69	20.37	16.71	13.50	8.41	3.49
T(K)	21.72	25.41	26.54	27.38	28.46	29.20

Table 4. Measured and calculated temperature (K) and N_2 concentration (%) in a CH_4-N_2O flame

HT(mm)	5	2	2	2
Flow (cm/s)	16.8	16.8	33.4	51.7

Equivalence ratio (F/O)

	0.3	0.4	0.5	1.0
TEXP	2550	2688	2782	2982 ± 52 (2%)
TCALC	2541	2654	2738	2920
CEXP	60	58	54	45 ± 3 (6%)
CCALC	62	60	58	51

Table 5. Temperature and N_2 concentration profile in a CH_4-N_2O flame (ϕ = 0.5) at a flow of 16.9 cm/s (TCALC = 2734K, CCALC = 58%)

Height above burner (mm)	Temperature (K)	Concentration (%)
3	2566	54.7
5	2559	46.5
10	2563	46.5
15	2491	51.6
20	2320	47.6
30	2090	51.9
40	1840	49.6
50	1820	50.5
60	1700	51.8

Table 6. Temperature and N_2 concentration profile in a CH_4-N_2O flame (ϕ = 0.5) at a flow of 33.4 cm/s (TCALC = 2734K, CCALC = 58%)

Height above burner (mm)	Temperature (K)	Concentration (%)
3	2782	54.2
10	2742	55.3
20	2713	50.8
30	2631	47.2
40	2521	51.1
50	2404	50.7
60	2282	51.4

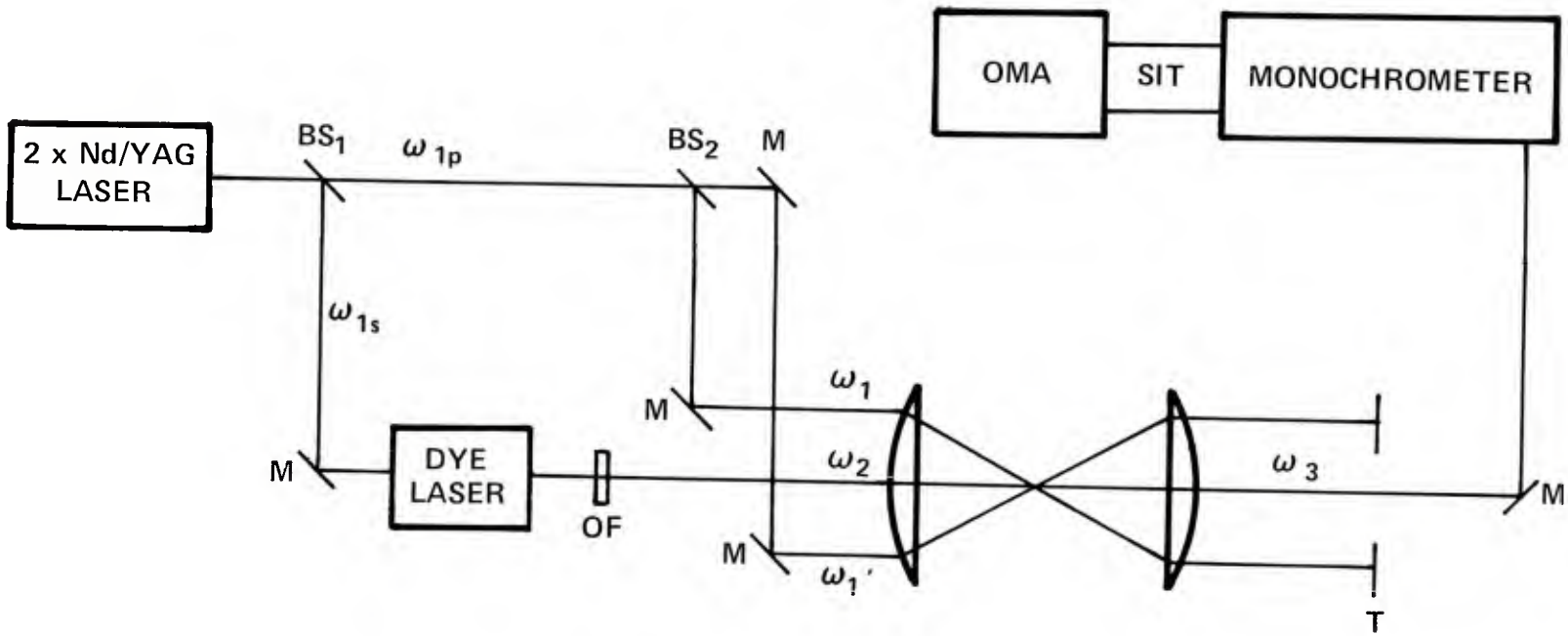

Figure 1. Nonplanar BOXCARS spectrometer where BS is a 50% beam splitter, M is a Mirror, OF is an optical flat rotable about its horizontal axis and T is a beam terminator

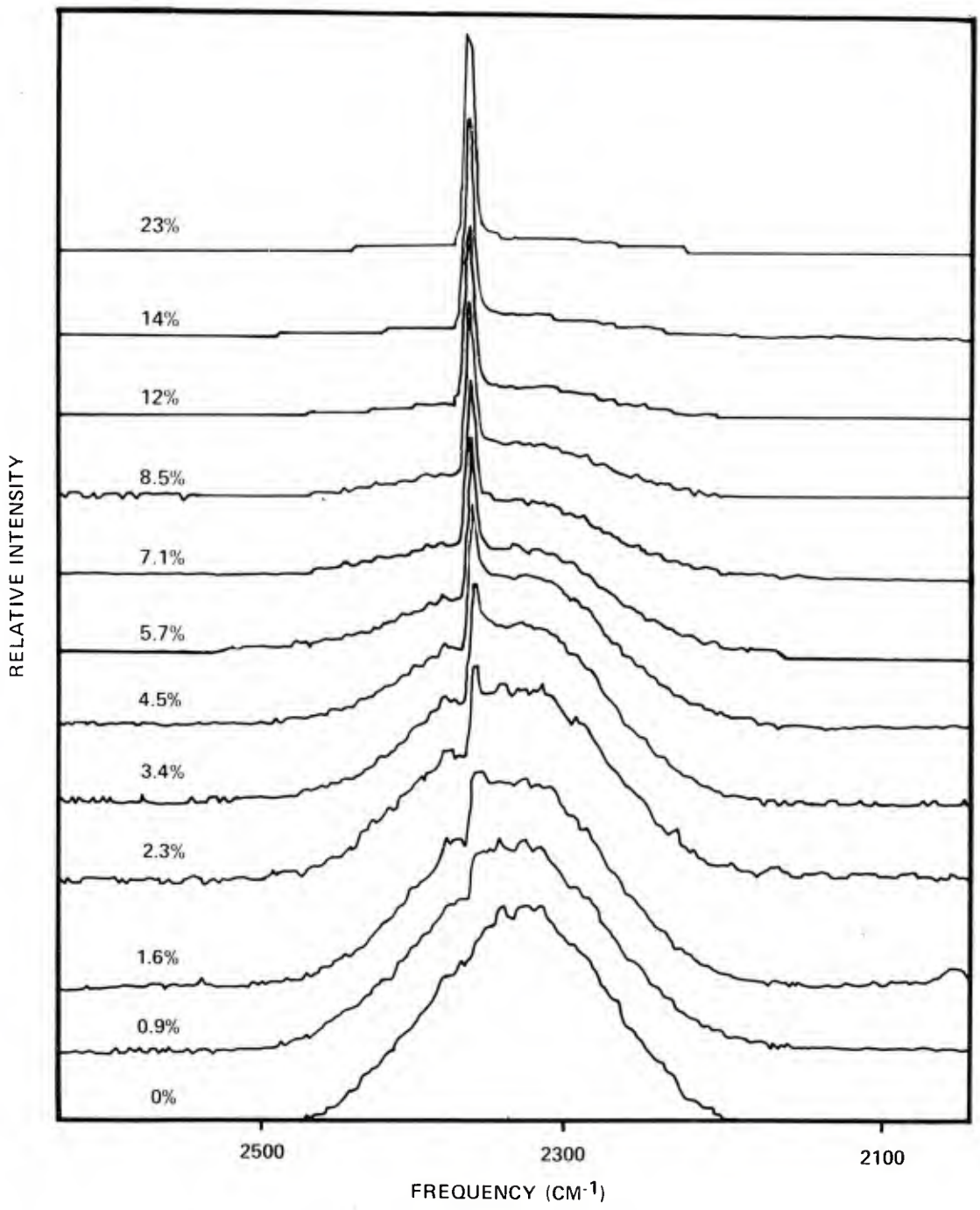

Figure 2. Normalized nitrogen CARS spectra from room temperature air/argon mixtures containing 0% to 23% air

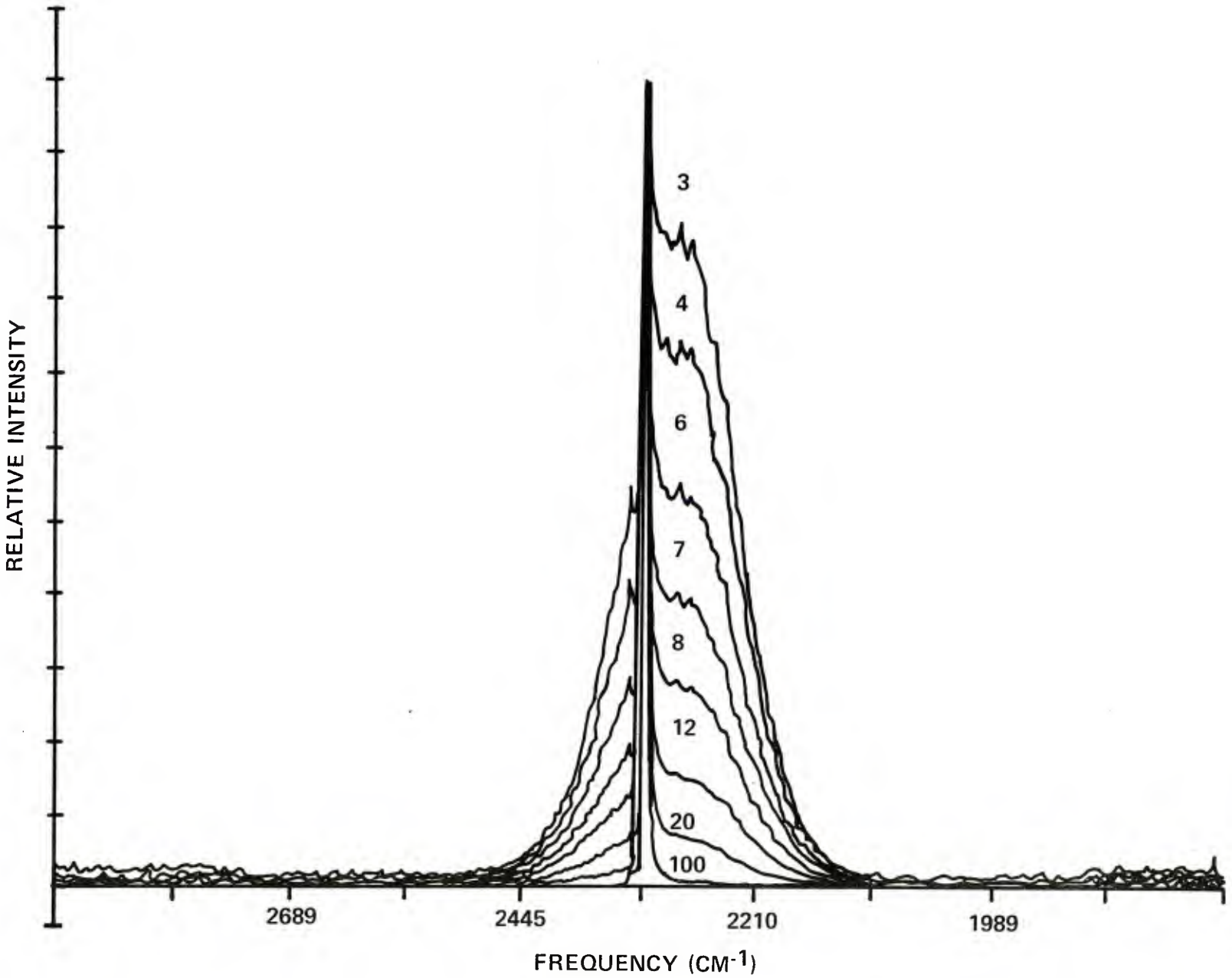

Figure 3. Normalized nitrogen CARS spectra from room temperature air/argon mixtures containing 3% to 100% air

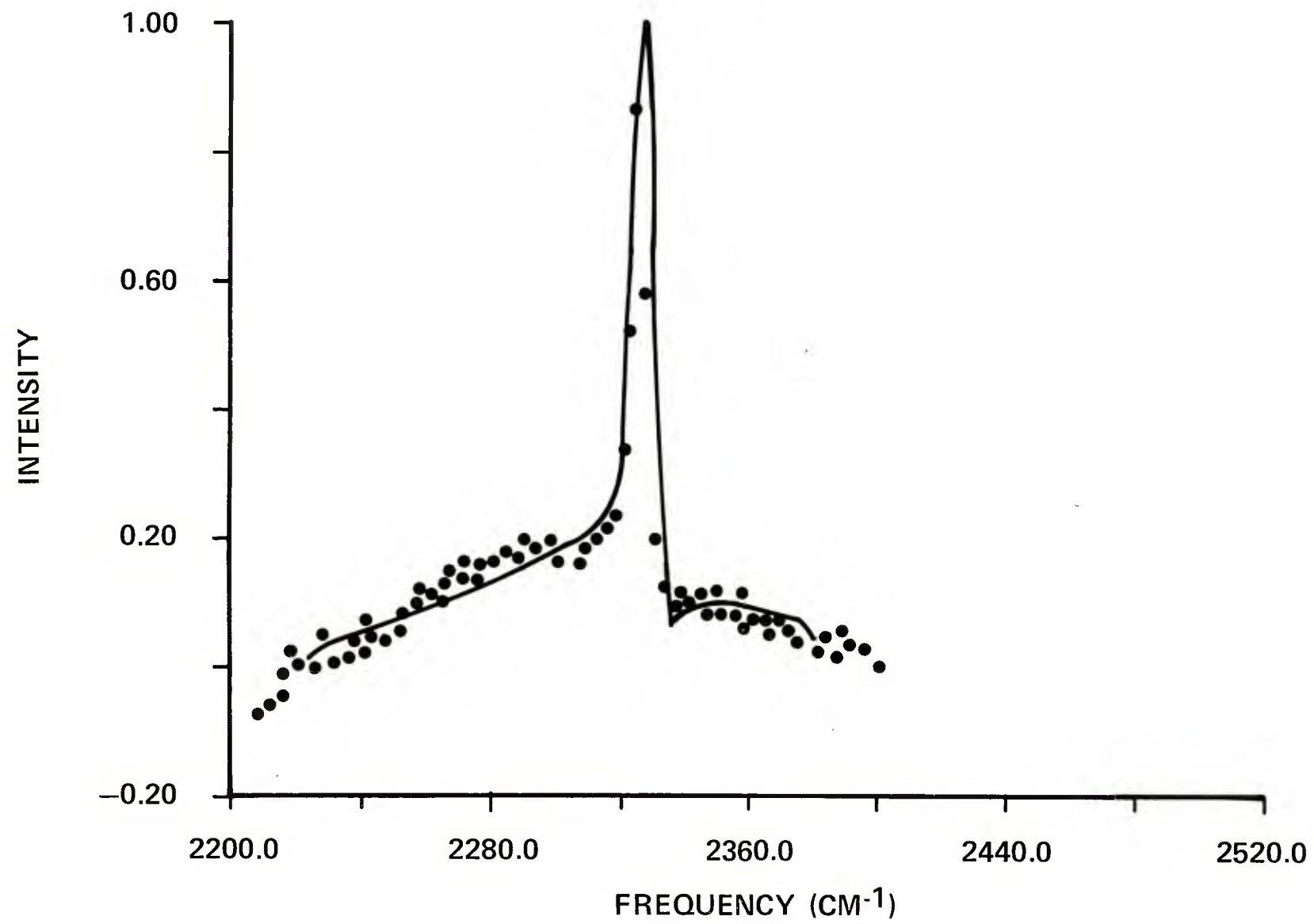

Figure 4. Experimental (·) and calculated N_2 CARS spectra at room temperature in a 9% air/argon mixture (nonplanar CARS)

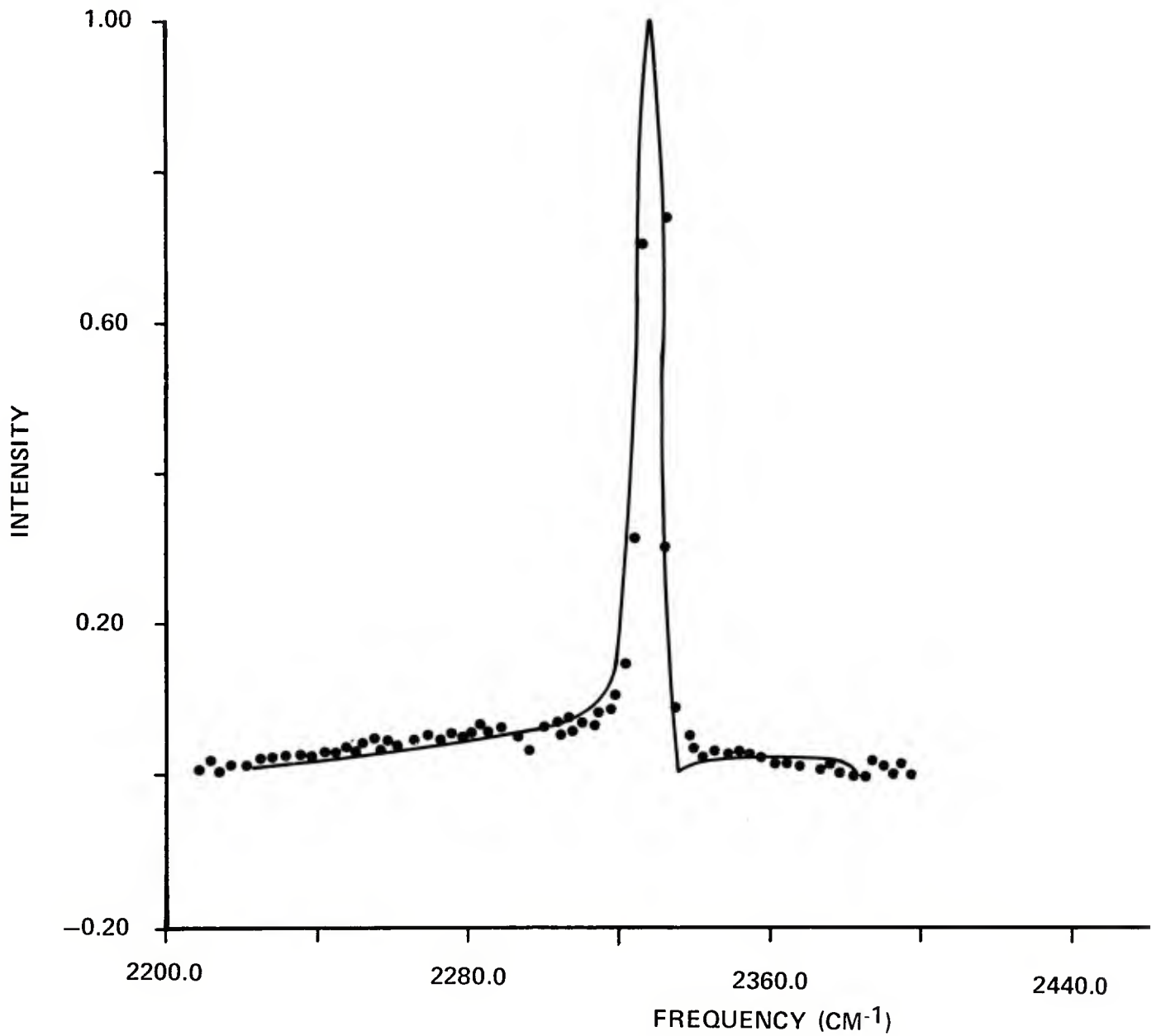

Figure 5. Experimental (·) and calculated N_2 CARS spectra at room temperature in a 20% air/argon mixture (nonplanar CARS)

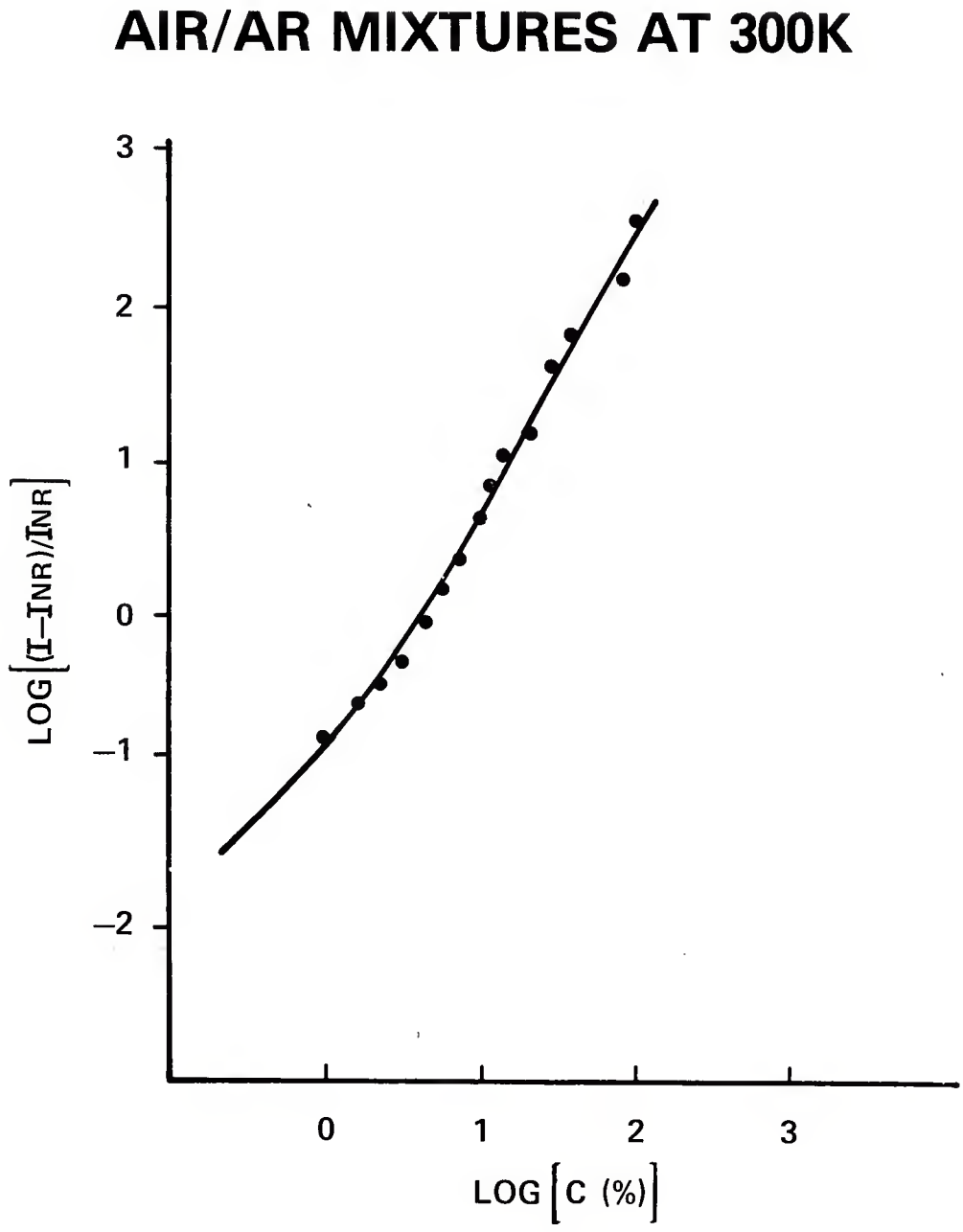

Figure 6. Experimental (•) and theoretical log $(I_{10} - I_{nr})/I_{nr})$ where I_{10} and I_{nr} are the maximum intensities of nitrogen Q_{10} and the nonresonant susceptibility versus log [C(%)]

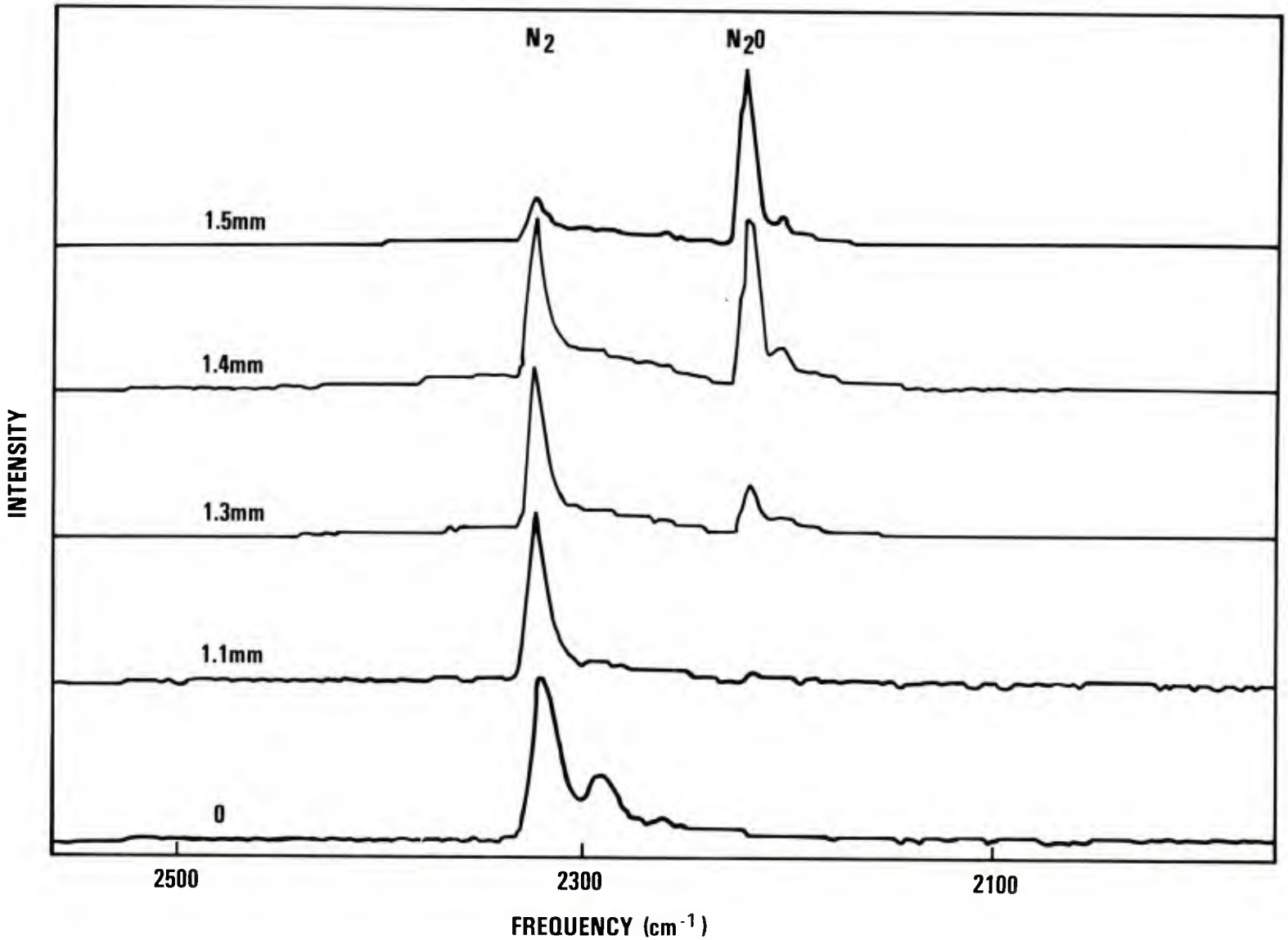

Figure 7. CARS spectra observed 1 mm above the burner head in a 0.27 CH_4-N_2O flame (the distance indicated is from centerline of the burner)

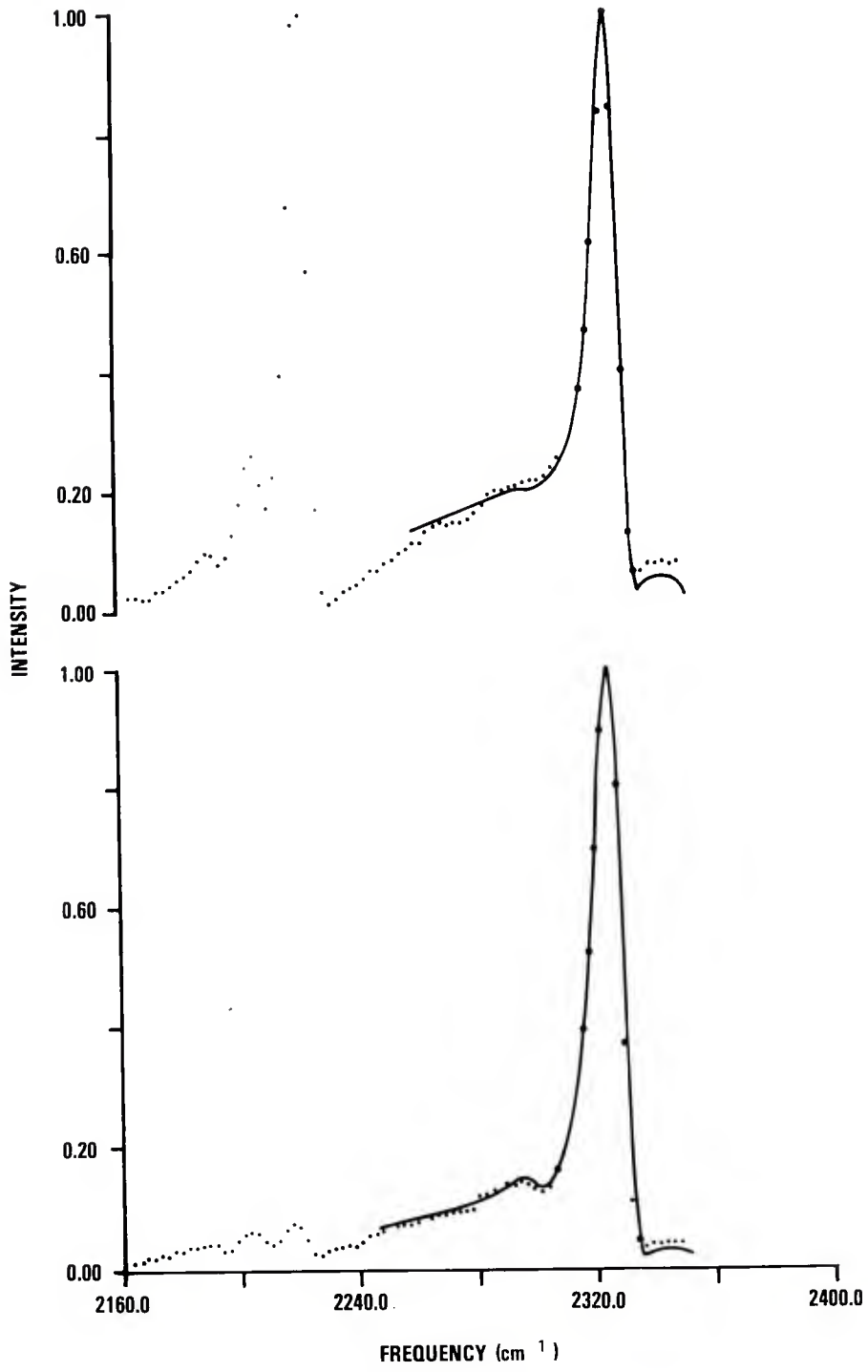

Figure 8. CARS spectra observed 1 mm above the burner head in a 0.27 CH_4-N_2O flame (•) compared to theoretical spectra (solid line), calculated at T = 800 K and C = 14% N_2 and T = 1200 and C = 20% N_2 for spectra obtained 1.40 (TOP SPECTRUM) and 1.14 mm (BOTTOM SPECTRUM) from the centerline of the flame, respectively

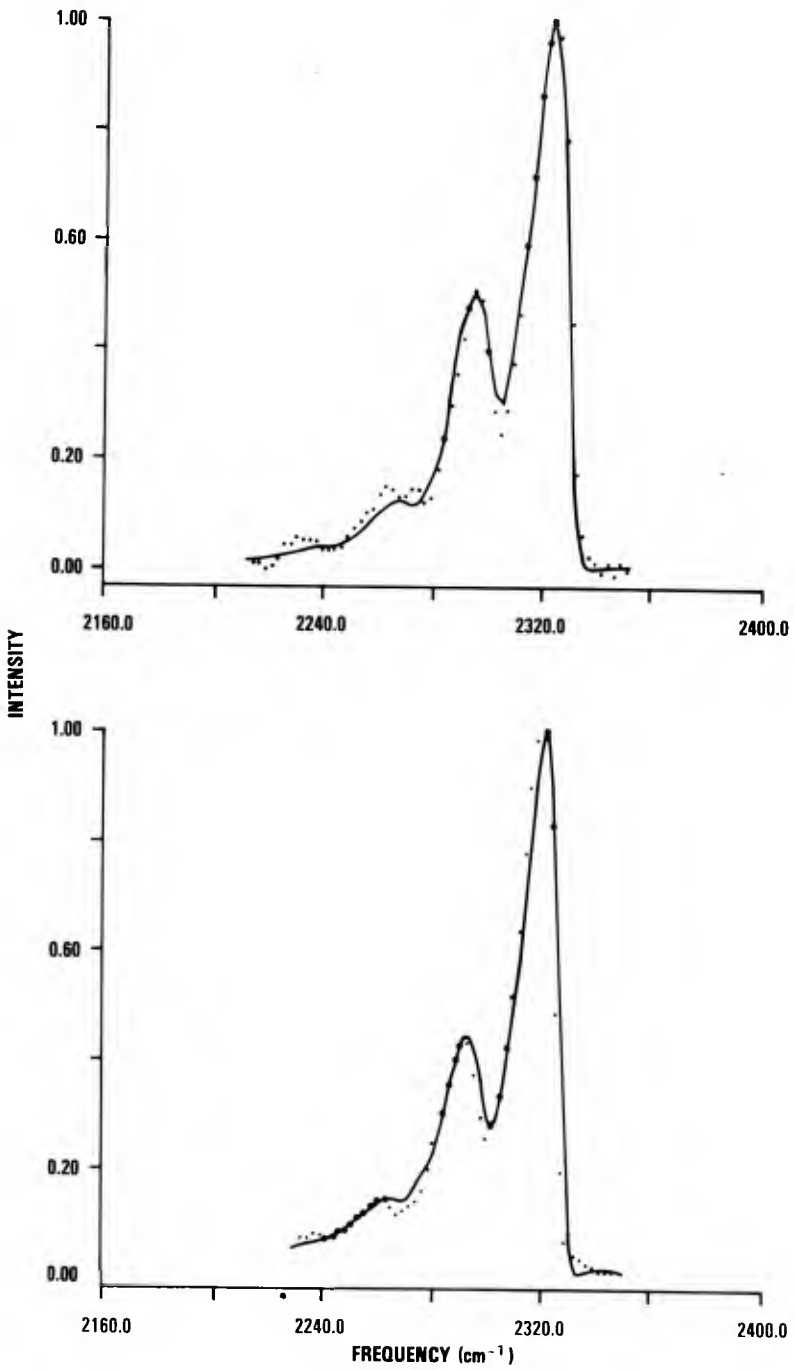

Figure 9. TOP SPECTRUM: N_2 CARS spectrum observed 2 mm above the centerline of 0.3 CH_4-N_2O flame (•) compared theoretical spectrum calculated at T = 2550 K and C = 62% N_2

BOTTOM SPECTRUM: N_2 CARS spectrum observed 1 mm above the centerline of a 0.27 CH_4-N flame (•) compared to theoretical spectrum calculated at T = 2300 K and C = 33% N_2

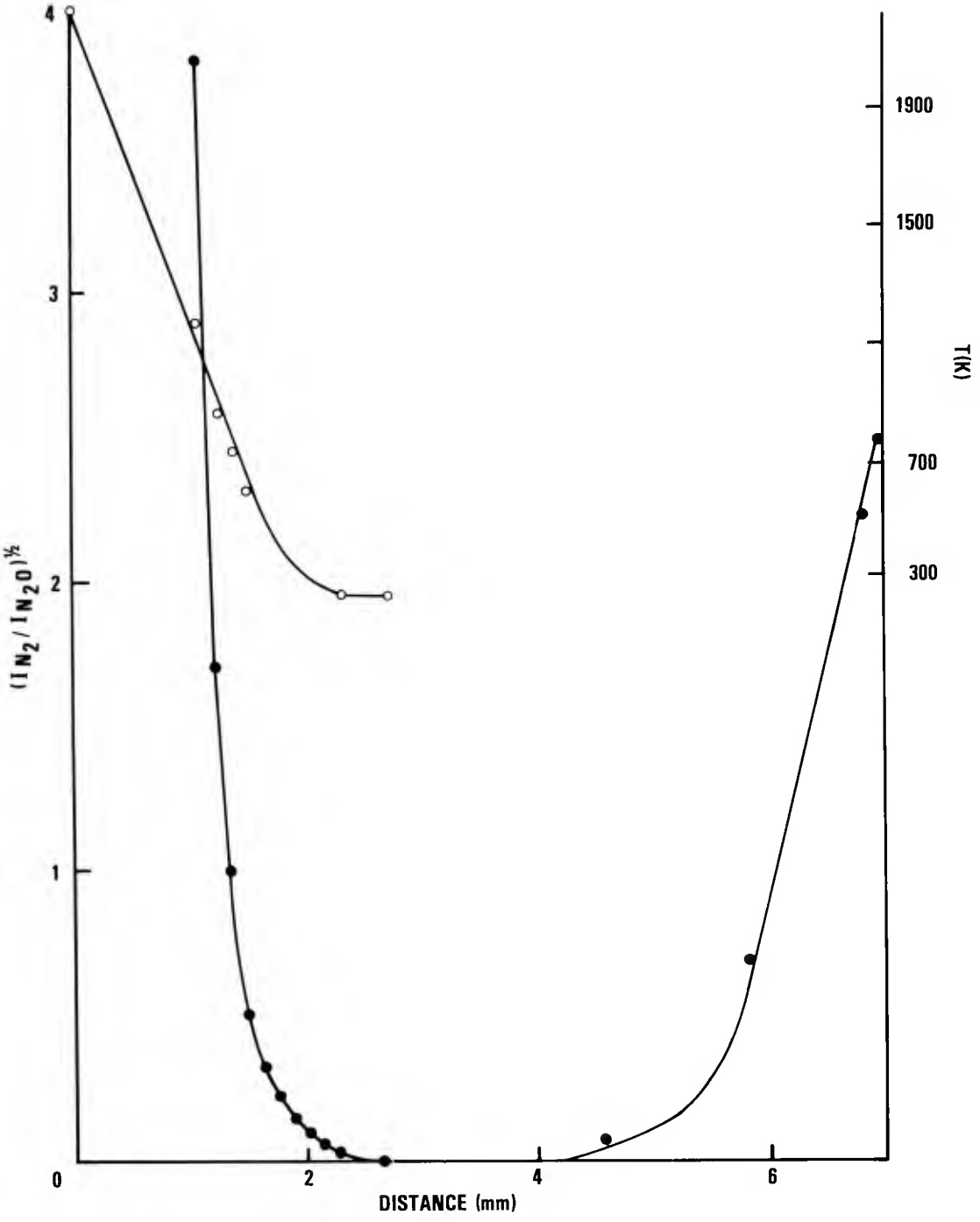

Figure 10. (I_{N_2}/I_{N_2O}) (•) obtained from CARS spectra taken 1 mm above the burner head of a 0.27 CH_4-N_2O flame and corresponding temperatures (•) versus distance from the centerline of the burner

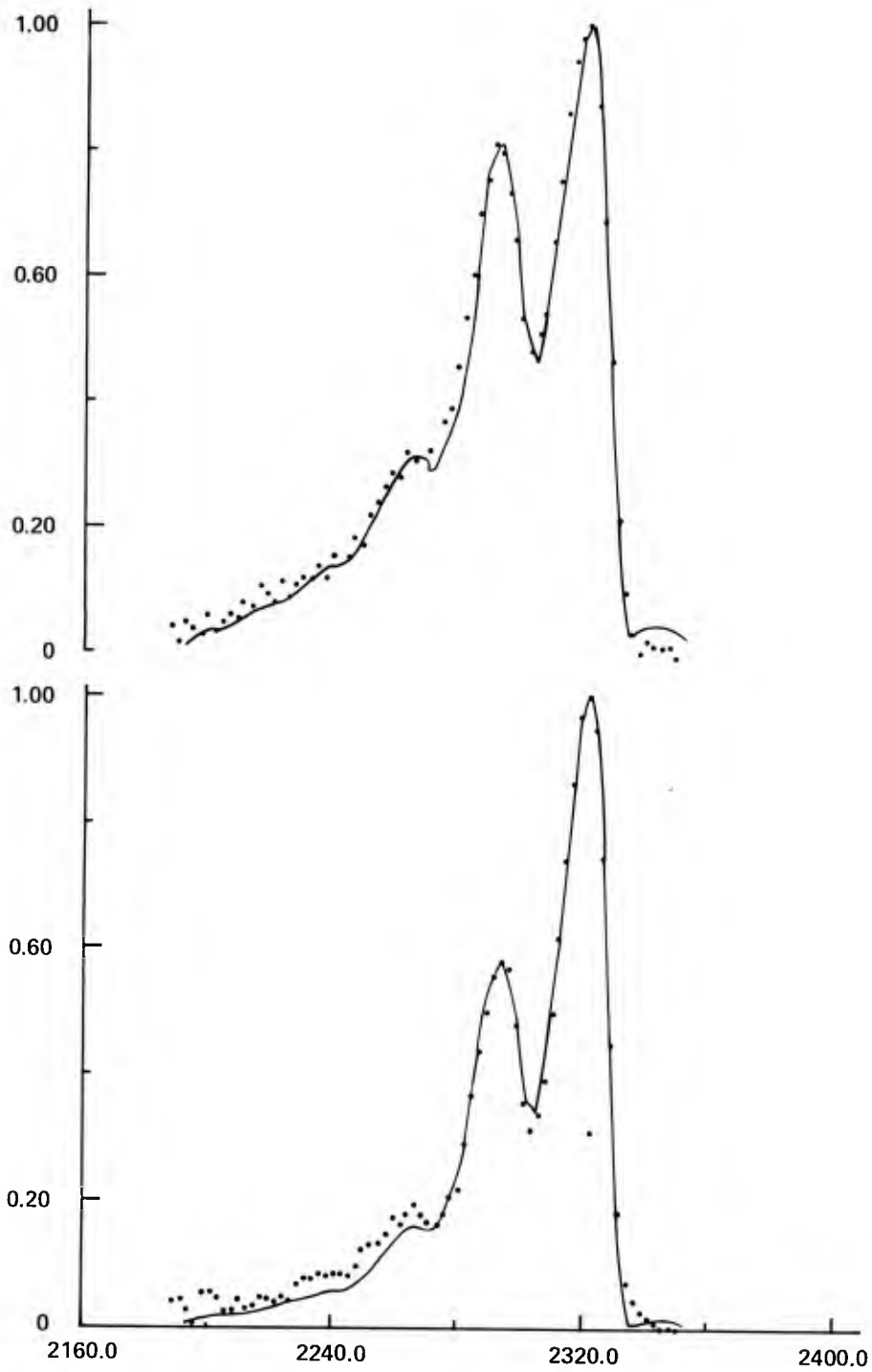

Figure 11. Experimental (•) and calculated N_2 CARS spectra (solid line) 2 mm above the centerline of the burner surface: BOTTOM, 0.4 flame; TOP, 1.0 flame

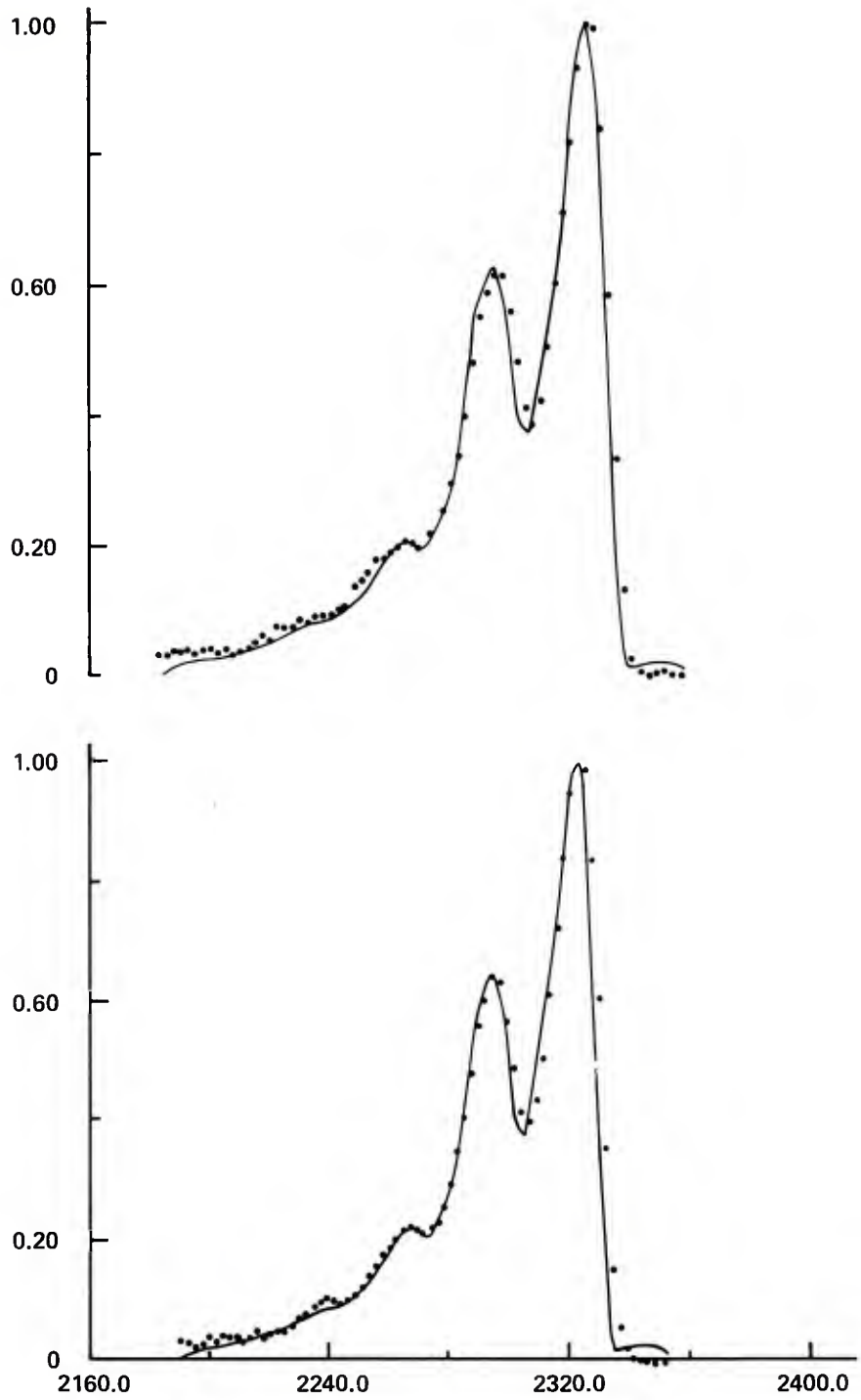

Figure 12. Experimental (•) and calculated N_2 CARS spectra (solid line) from a 0.5 flame at various distances from the burner surface: BOTTOM, 2 mm; TOP, 10 mm

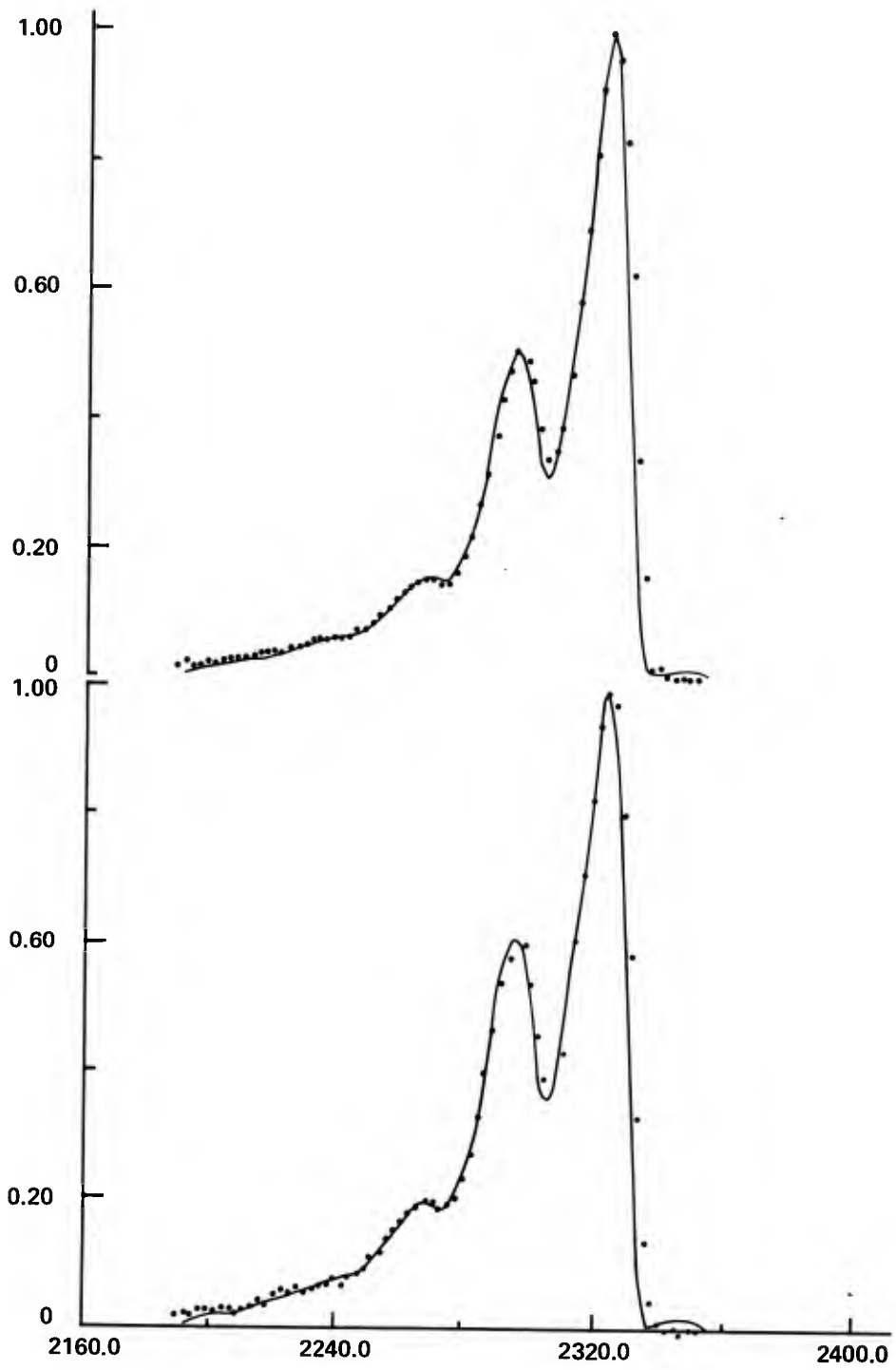

Figure 13. Experimental (•) and calculated N_2 CARS spectra (solid line) from 0.5 flame at various distances from the burner surface: BOTTOM, 20 mm; TOP, 40 mm

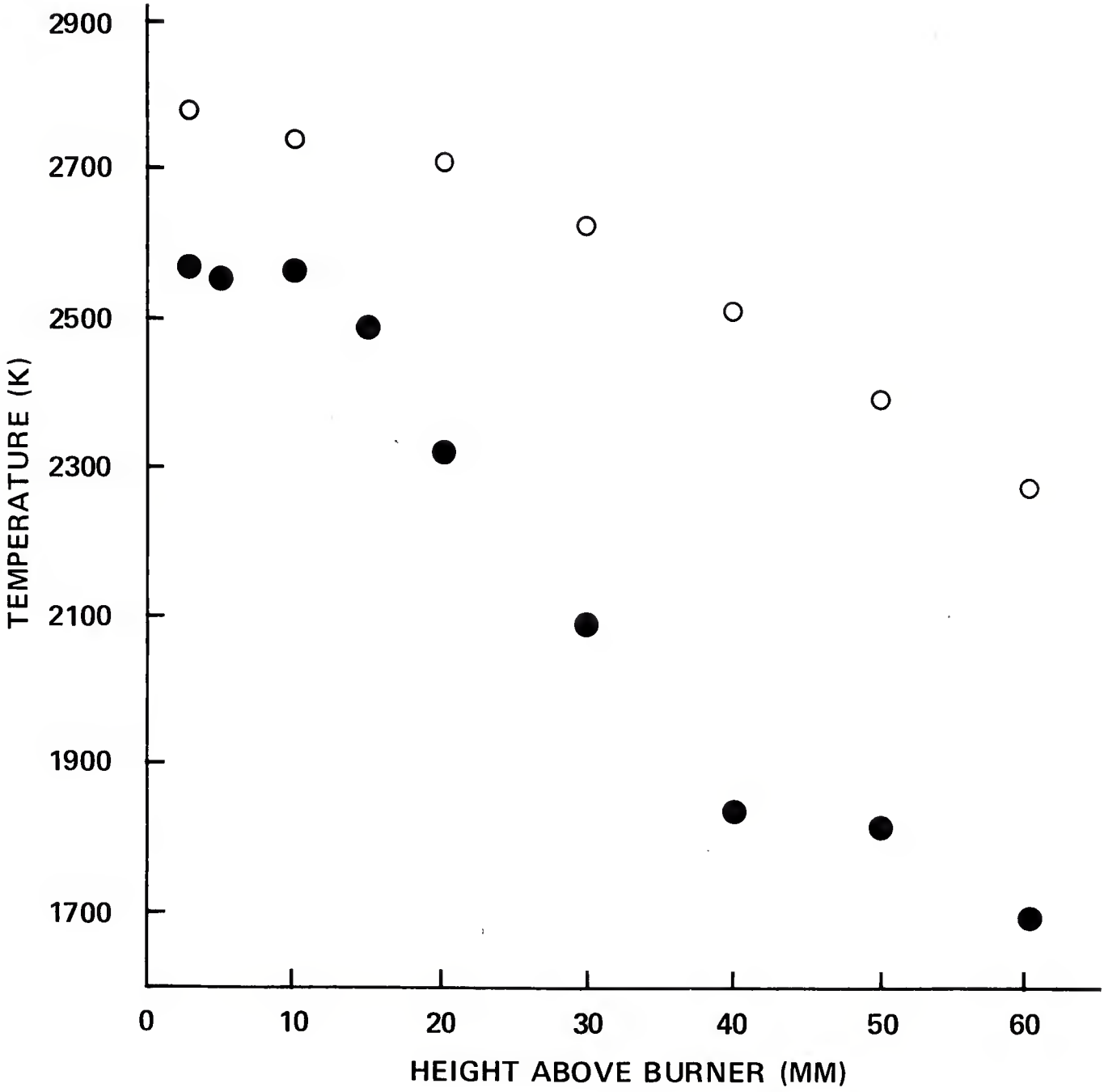

Figure 14. Temperature versus distance above the burner surface for a 0.5 flame at a flow of 16.8 (•) and 33.4 (o) cm/s

DISTRIBUTION LIST

Commander
U.S. Army Armament Research
and Development Command
ATTN: DRDAR-TSS (5)
DRDAR-GCL
DRDAR-LC, J. Frasier
DRDAR-LCA, A. Moss
DRDAR-LCA-G, J. Lannon
D. Downs
L. Harris (10)
T. Vladimiroff
A. Beardell
Y. Carignon
J. Fendell
K. Aron
E. Petro
DRDAR-LCE, R. Walker
P. Marinkas
C. Capellos
F. Owens
Dover, NJ 07801

Administrator
Defense Technical Information Center
ATTN: Accessions Division (12)
Cameron Station
Alexandria, VA 22314

Director
U.S. Army Materiel Systems
Analysis Activity
ATTN: DRXSY-MP
Aberdeen Proving Ground, MD 21005

Commander/Director
Chemical Systems Laboratory
U.S. Army Armament Research
and Development Command
ATTN: DRDAR-CLJ-L
DRDAR-CLB-PA
APG, Edgewood Area, MD 21010

Director
Ballistics Research Laboratory
U.S. Army Armament Research
and Development Command
ATTN: DRDAR-TSB-S
DRDAR-BLP, L. Watermier
A. Barrows
G. Adams
R. Fifer
M. Miller
T. Coffee
J. Heimeryl
C. Nelson
J. Vanderhoff
J. Anderson
Aberdeen Proving Ground, MD 21005

Chief
Benet Weapons Laboratory, LCWSL
U.S. Army Armament Research
and Development Command
ATTN: DRDAR-LCB-TL
Watervliet, NY 12189

Commander
U.S. Army Armament Materiel
Readiness Command
ATTN: DRSAR-LEP-L
Rock Island, IL 61299

Director
U.S. Army TRADOC Systems
Analysis Activity
ATTN: ATAA-SL
White Sands Missile Range, NM 88002

Director
Defense Advanced Research Projects
Agency
ATTN: LTC C. Buck
1400 Wilson Boulevard
Arlington, VA 22209

Director
Institute for Defense Analyses
ATTN: H. Wolfhard
R. T. Oliver
400 Army-Navy Drive
Arlington, VA 22202

Commander
U.S. Army Materiel Development
and Readiness Command
ATTN: DRCDMD-ST
5001 Eisenhower Avenue
Alexandria, VA 22333

Commander
U.S. Army Watervliet Arsenal
ATTN: SARWV-RD, R. Thierry
Watervliet, NY 12189

Commander
U.S. Army Aviation Research
and Development Command
ATTN: DRSAV-E
P.O. Box 209
St. Louis, MO 63166

Director
U.S. Army Air Mobility Research
and Development Laboratory
Ames Research Center
Moffett Field, CA 94035

Commander
U.S. Army Communications Research
and Development Command
ATTN: DRDCO-PPA-SA
Fort Monmouth, NJ 07703

Commander
U.S. Army Electronics Research
and Development Command
Technical Support Activity
ATTN: DELSD-L
Fort Monmouth, NJ 07703

Commander
U.S. Army Missile Command
ATTN: DRSMI-R
DRSMI-YDL
Redstone Arsenal, AL 35809

Commander
U.S. Army Natick Research
and Development Command
ATTN: DRXRE, D. Sieling
Natick, MA 01762

Commander
U.S. Army Tank Automotive Research
and Development Command
ATTN: DRDTA-UL
Warren, MI 48090

Commander
U.S. Army White Sands Missile Range
ATTN: STEWS-VT
White Sands Missile Range, NM 88002

Commander
U.S. Army Materials and
Mechanics Research Center
ATTN: DRXMR-ATL
Watertown, MA 02172

Commander
U.S. Army Research Office
ATTN: Technical Library
D. Squire
F. Schmiedeshaff
R. Ghirardelli
M. Ciftan
P.O. Box 12211
Research Triangle Park, NC 27706

Office of Naval Research
ATTN: Code 473
G. Neece
800 N. Quincy Street
Arlington, VA 22217

Commander
Naval Sea Systems Command
ATTN: J. W. Murrin, SEA-62R2
National Center
Bldg 2, Room 6E08
Washington, DC 20362

Commander
Naval Surface Weapons Center
ATTN: Library Branch, DX-21
Dahlgren, VA 22448

Commander
Naval Surface Weapons Center
ATTN: Code 240, S. J. Jacobs, J. Sharma
Code 730
Silver Spring, MD 20910

Commander
Naval Underwater Systems Center
Energy Conversion Department
ATTN: Code 5B331, R. S. Lazar
Newport, RI 02840

Commander
Naval Weapons Center
ATTN: R. Derr
C. Thelen
China Lake, CA 93555

Commander
Naval Research Laboratory
ATTN: Code 6180
Washington, DC 20375

Superintendent
Naval Postgraduate School
ATTN: Technical Library
D. Netzer
A. Fuhs
Monterey, CA 93940

Commander
Naval Ordnance Station
ATTN: Dr. Charles Dale
Technical Library
Indian Head, MD 20640

AFOSR
ATTN: J. F. Masi
B. T. Wolfson
D. Ball
L. Caveny
Bolling AFB, DC 20332

AFRPL (DYSC)
ATTN: D. George
J. N. Levine
Edwards AFB, CA 93523

National Bureau of Standards
ATTN: J. Hastie
T. Kashiwagi
H. Semerjian
M. Jacox
K. Smyth
J. Stevenson
Washington, DC 20234

Lockheed Palo Alto Research Laboratories
ATTN: Technical Information Center
3521 Hanover Street
Palo Alto, CA 94304

Aerojet Solid Propulsion Co.
ATTN: P. Micheli
Sacramento, CA 95813

ARO Incorporated
ATTN: N. Dougherty
Arnold AFS, TN 37389

Atlantic Research Corporation
ATTN: M. K. King
5390 Cherokee Avenue
Alexandria, VA 22314

AVCO Corporation
AVCO Everett Research Laboratory
Division
ATTN: D. Stickler
2385 Revere Beach Parkway
Everett, MA 02149

Calspan Corporation
ATTN: E. B. Fisher
A. P. Trippe
P.O. Box 400
Buffalo, NY 14221

Foster Miller Associates, Inc.
ATTN: A. J. Erickson
135 Second Avenue
Waltham, MA 02154

General Electric Company
Armament Department
ATTN: M. J. Bulman
Lakeside Avenue
Burlington, VT 05402

General Electric Company
Flight Propulsion Division
ATTN: Technical Library
Cincinnati, OH 45215

Hercules Incorporated
Alleghany Ballistic Lab
ATTN: R. Miller
Technical Library
Cumberland, MD 21501

Hercules Incorporated
Bacchus Works
ATTN: B. Isom
Magna, UT 84044

IITRI
ATTN: M. J. Klein
10 West 35th Street
Chicago, IL 60615

Olin Corporation
Badger Army Ammunition Plant
ATTN: J. Ramnarace
Baraboo, WI 53913

Olin Corporation
New Haven Plant
ATTN: R. L. Cook
D. W. Riefler
275 Winchester Avenue
New Haven, CT 06504

Paul Gough Associates, Inc.
ATTN: P. S. Gough
P.O. Box 1614
Portsmouth, NH 03801

Physics International Company
2700 Merced Street
Leandro, CA 94577

Pulsepower Systems, Inc.
ATTN: L. C. Elmore
815 American Street
San Carlos, CA 94070

Rockwell International Corp.
Rocketdyne Division
ATTN: C. Obert
J. E. Flanagan
A. Axeworthy
6633 Canoga Avenue
Canoga Park, CA 91304

Rockwell International Corp.
Rocketdyne Division
ATTN: W. Haymes
Technical Library
McGregor, TX 76657

Science Applications, Inc.
ATTN: R. B. Edelman
Combustion Dynamics and
Propulsion Division
23146 Cumorah Crest
Woodland Hills, CA 91364

Shock Hydrodynamics, Inc.
ATTN: W. H. Anderson
4710-16 Vineland Avenue
N. Hollywood, CA 91602

Thiokol Corporation
Elkton Division
ATTN: E. Sutton
Elkton, MD 21921

Thiokol Corporation
Huntsville Division
ATTN: D. Flanigan
R. Glick
Technical Library
Huntsville, AL 35807

Thiokol Corporation
Wasatch Division
ATTN: J. Peterson
Technical Library
P.O. Box 524
Brigham City, UT 84302

TRW Systems Group
ATTN: H. Korman
One Space Park
Redondo Beach, CA 90278

United Technologies
Chemical Systems Division
ATTN: R. Brown
Technical Library
P.O. Box 358
Sunnyvale, CA 94086

Universal Propulsion Co.
ATTN: H. J. McSpadden
1800 W. Deer Valley Road
Phoenix, AZ 85027

Battelle Memorial Institute
ATTN: Technical Library
R. Bartlett
505 King Avenue
Columbus, OH 43201

Brigham Young University
Department of Chemical Engineering
ATTN: M. W. Beckstead
Provo, UT 84601

California Institute of Technology
204 Karmar Lab
Mail Stop 301-46
ATTN: F. E. C. Culick
1201 E. California Street
Pasadena, CA 91125

Case Western Reserve University
Division of Aerospace Sciences
ATTN: J. Tien
Cleveland, OH 44135

Georgia Institute of Technology
School of Aerospace Engineering
ATTN: B. T. Zinn
E. Price
W. C. Strahle
Atlanta, GA 30332

Institute of Gas Technology
ATTN: D. Gidaspow
3424 S. State Street
Chicago, IL 60616

Johns Hopkins University/APL
Chemical Propulsion Information Agency
ATTN: T. Christian
Johns Hopkins Road
Laurel, MD 20810

Massachusetts Institute of Technology
Department of Mechanical Engineering
ATTN: T. Toong
Cambridge, MA 02139

Pennsylvania State University
Applied Research Laboratory
ATTN: G. M. Faeth
P.O. Box 30
State College, PA 16801

Pennsylvania State University
Department of Mechanical Engineering
ATTN: K. Kuo
University Park, PA 16801

Pennsylvania State University
Department of Material Sciences
ATTN: H. Palmer
University Park, PA 16801

Princeton Combustion Research
Laboratories
ATTN: M. Summerfield
N. Messina
1041 U.S. Highway One North
Princeton, NJ 08540

Princeton University
Forrestal Campus
ATTN: I. Glassman
F. Dryer
Technical Library
P.O. Box 710
Princeton, NJ 08540

Purdue University
School of Mechanical Engineering
ATTN: J. Osborn
S. N. B. Murthy
N. M. Laurendeau
TSPC Chaffee Hall
W. Lafayette, IN 47906

Rutgers State University
Department of Mechanical and
Aerospace Engineering
ATTN: S. Temkin
University Heights Campus
New Brunswick, NJ 08903

SRI International
ATTN: Technical Library
D. Crosley
J. Barker
D. Golden
333 Ravenswood Avenue
Menlo Park, CA 94025

Stevens Institute of Technology
Davidson Library
ATTN: R. McAlevy, III
Hoboken, NJ 07030

United Technology
ATTN: Alan Ecbreth
Robert Hall
Research Center
East Hartford, CT 06108

Commander
Naval Research Laboratory
Chemistry Division
ATTN: A. Harvey
Washington, DC 20375

General Motors Research Laboratory
ATTN: J. H. Bechtel
Warren, Michigan 48090

System Research Laboratory
ATTN: L. Goss
2600 Indian Ripple Rd
Dayton, Ohio 45440

Exxon Research and Engineering
ATTN: A. Dean
M. Chou
P.O. Box 45
Linden, NJ 07036

Ford Motor Company
Research Staff
ATTN: K. Marko
L. Rimai
Dearborn, Michigan 48120

Sandia Laboratories
Applied Physics Division I
ATTN: L. Rahn
D. Stephenson
Livermore, CA 94550

Rensselaer Polytechnic Institute
Dept. of Chem. Engineering
ATTN: A. Fontijn
Troy, NY 12181

University of California,
San Diego
Ames Department
ATTN: F. Williams
P.O. Box 109
La Jolla, CA 92037

University of California
Dept. of Mechanical Eng.
ATTN: J. W. Daily
Berkeley, CA 94720

Univ. of Dayton
University of Dayton Research Inst.
Dayton, OH 45406

University of Florida
Dept. of Chemistry
ATTN: J. Winefordner
Gainesville, Florida 32601

University of Illinois
Dept. of Mechanical Eng.
ATTN: H. Krier
144 MEB, 1206 W. Green St.
Urbana, IL 61801

University of Minnesota
Dept. of Mechanical Eng.
ATTN: E. Fletcher
Minneapolis, MN 55455

University of California,
Santa Barbara
Quantum Institute
ATTN: K. Schofield
M. Steinberg
Santa Barbara, CA 93106

University of Southern California
Department of Chemistry
ATTN: S. Benson
Los Angeles, CA 90007

Stanford University
Department of Mech. Eng.
ATTN: R. Hanson
Stanford, CA 93106

University of Texas
Department of Chemistry
ATTN: W. Gardiner
H. Schaefer
Austin, TX 78712

University of Utah
Dept. of Chemical Engineering
ATTN: A. Baer
G. Flandro
Salt Lake City, UT 84112